Construction and Building Materials 401 (2023) 132721

Contents lists available at ScienceDirect

Construction and Building Materials

journal homepage: www.elsevier.com/locate/conbuildmat

Spatial correlation and pore morphology analysis of limestone calcined clay cement (LC^3) via machine learning and image-based characterisation

Hao Sui, Wei Wang, Junlin Lin, Zhao Qing Tang, Der-Shen Yang, Wenhui Duan *

Department of Civil Engineering, Monash University, Clayton, Victoria 3800, Australia

ARTICLE INFO

Keywords:
Limestone calcined clay cement (LC^3)
Machine learning
Microstructure
Image characterization
Spatial correlation
Pore morphology

ABSTRACT

Comprehending the microstructure of LC^3 is of paramount importance since it governs majority properties of cement. Here, we investigate the spatial correlation and pore morphology of LC^3, revealing microstructural refinement effects through deep learning and image-based characterisation. A deep learning model was developed to characterise the spatial correlation of the local features of 28-day LC^3 with optimised resolution and physical image size, identifying a lower probability of connected pores occurring but a higher likelihood of connected solid particles in LC^3 than in OPC. A 33% lower maximum correlation revealed by two-point correlation analysis inferred that LC^3 possessed a smaller RVE size and increased packing density. The pore morphological analysis based on BSE images indicated a higher hydration rate and pore deformation in LC^3. These findings demonstrate the microstructural refinement mechanisms of LC^3 but also lay the foundation for localised microstructural characterisation of cementitious materials with the potential to complement existing traditional analyses.

1. Introduction

Supplementary cementitious materials, including calcined clay (CC), are low-carbon solutions by substituting clinker for cement or replacing cement in the concrete mixture to reduce a relatively large amount of carbon dioxide emitted during clinker production [1–4]. Recently, a new type of ternary blended cement, limestone calcined clay cement (LC^3), has been developed with a 50% clinker replacement ratio [5,6]. As a high-potential green solution for the cement industry, LC^3 can also achieve better mechanical performance and superior durability compared with ordinary Portland cement (OPC) via microstructure modification [7,8].

LC^3 is a relatively new ternary blended cement where most of the existing research topics are focused on their microstructure, mainly involving the investigation of porosity and pore size distribution [9,10]. Scrivener et al. reported that increasing the kaolinite content reduced porosity from 3 days, which indicated that the pozzolanic reaction at early hydration ages is the main factor contributing to the microstructural refinement of LC^3 [11]. Sui et al. [12] quantitatively analysed the 28-day localised porosity surrounding the solid phases in LC^3 and found it was only 60% by volume compared with OPC, owing to the pozzolanic and synergetic reaction between CC and limestone (LS), increasing the formation of the AFm phases, such as hemi- and mono-carboaluminates. Zunino and Scrivener investigated the long-term microstructural development and refinement of LC^3 up to 3 years hydration, reporting up to 50% decrease in pore size, mainly due to the formation of carboaluminite and strätlingite phases and the transformation of hemicarboaluminites formed from the early hydration age to monocarboaluminates [13].

However, the microstructural refinement of cementitious materials depends not only on porosity and pore size [14] because cement composites are typically random heterogeneous materials, and pore size distribution does not contain any spatial information on cementitious materials [15,16]. Recent research on OPC composites has reported that the spatial correlation of pore clusters, the spatial correlation of microstructural features and local morphological descriptors (i.e., pore shape) also contribute to the refinement of the cement microstructure, subsequently critically affecting the mechanical and durability performance [17]. Research has shown that cementitious composites with a lower correlation distance tend to have superior mechanical performance due to a more homogenous microstructure and reduced stress concentration [18,19], highlighting the importance of the analysis and understanding of the spatial correlation of cementitious materials. Specifically, it has been reported that the spatial correlation of the

* Corresponding author.
E-mail address: wenhui.duan@monash.edu (W. Duan).

https://doi.org/10.1016/j.conbuildmat.2023.132721
Received 2 May 2023; Received in revised form 17 July 2023; Accepted 31 July 2023
Available online 12 August 2023

microstructure in cementitious materials can be quantitatively characterised by statistical functions, which essentially capture the degree of spatial correlation among different locations [20], such as the two-point correlation function [21]. Two-point correlation is a geometric concept widely adopted in microstructural analysis [22], and it describes the influence of any given point in an image on other points with regard to their distance (correlation distance) [23,24].

The two-point correlation function alone, however, cannot sufficiently and uniquely characterise the spatial correlation because it fails to give sufficient consideration to the influences on the spatial distribution of solid phases and pore shape [15,21]. Wang et al. [25] used spatial distribution analysis to characterise the microstructural refinement of cement composites via quantitative nanomechanical mapping (QNM). The microstructural densification and uniformity from incorporating graphene oxide in cement paste reduced the stress concentration and increased mechanical strength up to 90% [25]. In addition, the pore shape descriptor, solidity, illustrates the edge of cement particles and the hydration products on the wall of the pores, which are influenced by the hydration degree and packing of cementitious materials, respectively [26]. An example of utilising solidity is the study by Liu et al., who demonstrated that solidity could illustrate the overall densification of the cement microstructure with hydration processing, indicating that microstructural refinement effects can be analysed by pore shape [27].

Understanding the microstructural refinement mechanism is one of the primary challenges in the analysis of cementitious materials [28]. Conventional statistical approaches aforementioned cannot efficiently identify and extract the nano-to-microscale changes in cementitious composites. Although LC^3 is an OPC-based cement, several studies report that the formation of LC^3's microstructure differs from that of OPC [29–31], such as different types of hydration products [29] and a lower gel–space ratio [32]. Therefore, the detailed microstructural refinement mechanisms of LC^3 still need to be investigated using advanced tools (e.g., artificial intelligence-based approach).

Machine learning encompasses a wide array of techniques that exhibit diverse applications, each presenting distinct strengths and weaknesses. Different approaches offer unique advantages tailored to specific tasks. As an advanced machine learning method, deep neural networks (DNN) can provide the inner correlation via multiple processing layer artificial neural networks [33,34] and distinguish the most significant characteristics from redundant or duplicate input data [35], which previously mentioned methods could not achieve. Existing studies have reported the feasibility and accuracy of DNNs for predicting microstructure-based properties, such as compressive strength [36], elastic modulus [37] and phase segmentation [38], demonstrating the ability to show the microstructural changes in cementitious materials. DNN is able to learn from the input data (i.e., cement microstructure images) and extract the most representative and unique features with minimal interfering factors to reveal the potential microstructural refinement mechanisms (i.e., spatial correlation between different phases) [35,39].

Moreover, DNN is known for its cost efficiency, as it requires low computational resources [40–42]. The great effectiveness of a DNN was exemplified in a study by Wang et al. in which the incorporation of nano modifications within the random heterogeneous microstructure revealed distinctive features that were effectively learned by DNN, thereby elucidating the refinement mechanisms associated with spatial heterogeneity in the hardened cement microstructure [43]. Therefore, we expected that a DNN would distinguish the most representative features from cement microstructure images, contributing to a deeper understanding of spatial correlation and revealing reliable but unanticipated findings on the microstructural refinement mechanisms of LC^3.

To our knowledge, this study investigated the spatial correlation and pore morphology of LC^3 to reveal the microstructural refinement effects, which have not been done previously. A deep learning approach was adopted to assist in understanding mechanical and durability-related performance. Image-based microstructural analysis and visualisation were used to demonstrate the modification of LC^3's microstructure by statistical pore diameter characterisation and morphology of the pores. Both BSE and micro-CT images were adopted for DNN training to find an optimised physical image size and resolution with the lowest computational costs. Upon conducting the DNN training, the characteristic features were visualised to reveal the probability of the occurrence of pores and solid phases. Two-point correlation function and QNM were then applied to further explain the influences of the spatial correlation of pores and solid phases between LC^3 and OPC. These findings not only quantified the microstructural refinement of LC^3 but also created a foundation for localised microstructural characterisation of cementitious materials. Thus, our study results could promote the understanding of the structure–property link in LC^3 with the potential to complement existing traditional cementitious material microstructural analyses.

2. Materials and methods

2.1. Materials

The CC mainly contained muscovite, quartz, and 58% kaolinite from kaolin tailings in Guanxi Zhuang Autonomous Region, China. OPC that met the requirements of Australian Standard AS 3972 was used to prepare the cement pastes in this study. The chemical composition of the CC and OPC is presented in Table 1. Polycarboxylic-based superplasticiser purchased from Sika Australia Pty Ltd was used to adjust the workability of the LC^3 paste.

Fig. 1 demonstrates the particle size distribution of cement, CC, and LS. In terms of the calcination process, an industrial rotary kiln at 800 °C was used to maintain the high activity of the CC.

OPC and LC^3 pastes were prepared to examine the microstructure, following the requirements of Australia Standard AS 3972 [44], and the mixes have been listed in Table 2. All samples were demoulded after 24 h and immersed in saturated $Ca(OH)_2$ solution until 28 days. The hardened samples were then immersed in isopropanol to arrest the hydration for microstructure characterisation.

2.2. Image acquisition and preparation

Two different microstructure analysis techniques, metal intrusion-based backscattered electron (BSE) imaging and X-ray computed tomography (CT) technique, were applied to observe the microstructure of OPC and LC^3 pastes at the curing age of 28 days and obtain the original dataset for DNN model training.

To acquire BSE images that accurately displayed the microstructure of the cementitious materials, a low melting point metal intrusion technique, Field's metal intrusion porosimetry (FMIP), was used. Three steps are essential for the FMIP technique to enable observation of the morphology. Cubic samples of ≈5 × 5 × 5 mm were taken from the core of each cement sample. Field's metal was put into a titanium alloy holder to be heated and the holder's surface temperature was maintained at 80 ± 5 °C during the experiment to ensure that the metal was kept in a liquid state the whole time. After putting the cement sample into the holder, a Shimadzu AG-X test machine was used to gradually pressurise to 400 MPa at a constant pressure increase of 11.2 MPa/min and held for another 30 min at 400 MPa to guarantee the pores of the cement sample had been adequately intruded. Corresponding to the 400 MPa loading pressure, the minimum reachable pore diameter was ≈3.6 nm following Washburn's equation [45]. Then, the holder was cooled to room temperature under this pressure to ensure the Field's metal became solid before removing the sample. The sample was impregnated with epoxy resin and polished to reduce metal extrusion during scanning electron microscopy (SEM) and improve image quality. The polishing process was performed with four different grades of silicon carbide sandpapers (125 μm, 58.5 μm, 25.8 μm, and 15.3 μm) and four grades of diamond/ethanol polishing suspension (6 μm, 1 μm, 0.25 μm, and 0.1

Table 1
Chemical composition of the calcined clay and OPC from X-ray fluorescence (weight %).

Compounds (%)	SiO_2	Al_2O_3	Fe_2O_3	CaO	MgO	SO_3	K_2O	Na_2O	TiO_2	LOI
CC	57.20	38.56	1.02	0.01	0.20	0.08	2.54	0.23	0.14	0.02
Cement	24.42	4.90	2.22	61.93	1.86	3.69	0.39	0.11	0.29	0.19

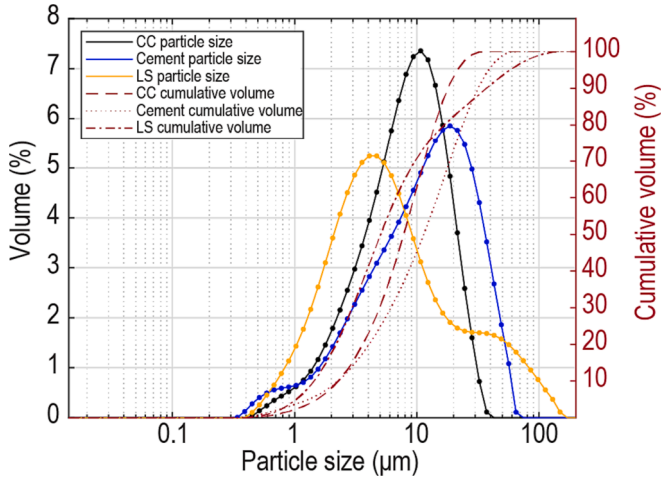

Fig. 1. Particle size distribution of calcined clay, cement, and limestone.

Table 2
Mix proportion of OPC and LC^3 pastes.

Sample	Clinker	Calcined clay	Limestone	Gypsum	w/b
LC^3	50%	30%	15%	5%	0.5
OPC	95%	0	0	5%	0.5

μm). The samples were thoroughly cleaned ultrasonically three times with ethanol to guarantee that no larger particles remained on the sample's surface before the finer polishing process.

For BSE imaging, a 10 nm carbon layer was coated on the surface of each sample before imaging in order to avoid the charging effect and improve image quality. An FEI Nova 450 FEG-SEM machine with 5 keV low-energy electrons and 10 μs electron beam dwell time was used with a scanning area of 5.461×10^6 μm^2 for each sample at × 1000 magnification. At this magnification, one pixel represented approximately 67 nm. Ten original BSE images at random non-overlapping positions for each sample were taken to acquire > 50,000 pore profiles. The high contrast BSE images can capture the solid phases and pore structure due to the high differences in atomic numbers between cement solids and Field's metal. The images obtained by SEM were converted into an 8-bit grayscale and characterised with multifunctional image processing software (ImageJ) [46]. The grey-level threshold segmentation was determined by the K means algorithm in MATLAB software [47–49]. Other detailed image characterisation processes and reliability verification are described elsewhere [12,26,50].

As for micro-CT imaging, a ZEISS Xradia XRM520Versa high-resolution X-ray computed tomography machine with a scanning size sample of ≈2 × 2 × 2 mm was used for micro-CT image acquisition. The pixel size of the micro-CT images was approximately 0.7 μm. The scanning parameters applied in this study, including power, X-ray energy, detector, detector to sample distance exposure time and camera binning, were set to 10 W, 140 keV, 4 × detector, 200 mm, 7.0 s and 4, respectively. The images acquired from the micro-CT process were reconstructed and characterised in MATLAB software. The segmentation and imaging characterisation processes are similar to the FMIP imaging process. The data were then exported to Blender software for microstructural visualisation.

2.3. Deep learning model and visualisation

Upon acquiring BSE and micro-CT images, the deep learning model was adopted to analyse the differences in spatial correlation between LC^3 and OPC pastes. The input data obtained from BSE and micro-CT images were separated into two datasets: binarised BSE and micro-CT images. In each dataset, every image was divided and categorised into squares with different physical sizes (6.76 μm, 13.52 μm, 33.8 μm, 54.08 μm, 67.6 μm, 81.12 μm and 101.4 μm), but 6.76 μm images were not characterised for micro-CT, because of the resolution limit of micro-CT images; that is, 6.76 μm did not contain enough features to be analysed in the DNN. Next, each category of binarised BSE and micro-CT images was fixed to 200 × 200 pixels for each physical size. As for DNN training, 2000 randomly selected images were extracted from each category. Specifically, each physical size sample (category) contained 1800 images in the training set, and the remaining 200 images were the test set to verify the accuracy of the classification. Two categories were randomly selected from all input images for the training and verifying process.

The adopted DNN model [43] contained seven convolutional layers followed by seven batch normalization layers and seven ReLU layers, showing optimal classification accuracy and training speed. Unlike the original neural network, the input data of the DNN used in this study did not remove nanoscale features because we were concerned that the micro-CT images did not have most of the nano-features compared with the BSE images. The binarised images covering a total area of 8×10^5 μm^2 were twice as large as the input areas of the previous work [43]. The image coverage area in this study exceeded the recommended size for 2D cementitious composite image microstructural analyses [27,51].

A developed layer-wise relevance propagation, deep Taylor decomposition, was used to decompose and explain the classification decisions of the DNN in this study. As a method to determine the threshold for a given value image, Isodata thresholding [52] was used to distinguish pores and solids on the binarised images. The details of deep Taylor decomposition and statistical characterisation of binarised BSE images have been described in our previous work [43].

2.4. Spatial correlation characterisation

The correlation distance obtained from the two-point correlation function can be used to demonstrate the spatial correlation of the cement microstructure. The cement microstructure is divided into pores and solid areas for each binarised BSE image. Therefore, the microstructure can be described as follows:

$$S(i,j) = \begin{cases} 1 if ij \in solid areas \\ 0 if ij \in Pore areas \end{cases} \quad (1)$$

where S denotes the square lattice and ij is the pixel index and determines the location within the image. Given two random phases i and j, the $S(i,j)$ can be converted with the location vector and the two-point correlation function (S_2) defined as:

$$S_2(i,j) = \langle S(i,j)S(i+x_i, j+x_j)\rangle \quad (2)$$

where x_i and x_j indicate the position of two points extracted from random phases i and j, and the angular brackets derive the probability of x_i and x_j both from the solid phase. The $S(i,j)$ can be replaced by the function $P(i,j)$, which determines the probability of the pixels $i$and$j$ being solid. By only considering the distance (r) between any pair of phases to

simplify the function, the function can be denoted as equation (3) and illustrated in Fig. 2:

$$S_2(r) = \langle P(i,j)P(i+r,j+r)\rangle \quad (3)$$

As for QNM tests, all hardened cement paste samples were cut into small pieces of 5 × 5 × 5 mm cubic, mounted in epoxy and polished with sandpaper and diamond pastes (for details, see Section 2.2). The nanomechanical properties of the cement paste were measured on the polished cross-sections using a Bruker's Dimension iCon® atomic force microscope with PeakForce QNM mode. A diamond tip (PDNISP-HS) with a spring constant of 338.33 N/m and a deflection sensitivity of 193.8 nm/V was used, and a HOPG sample was used to calibrate the radius of the diamond tip. The scanning areas were selected from the middle of the cement paste samples.

2.5. Pore shape characterisation

The shape descriptor, solidity, a geometric property describing a shape, defined as the percentage of a convex hull with an interior angle $< 180°$ that fully encapsulates the pore [26]. The solidity of a pore is related to the formation of hydration products and can be calculated for a non-circular pore with a certain area as:

$$Solidity = \frac{A}{convex\,A} \quad (4)$$

where A is the area of a pore, and *convex A* is the area of a convex hull that fully encapsulates the pore.

3. Results and discussion

In this section, the microstructure of 28-day LC^3 is compared with OPC to reveal the microstructural refinement effect on spatial correlation and pore morphology. First, two imaging techniques (i.e., BSE and micro-CT) were adopted to analyse the statistical pore size distribution. Second, images from both techniques were used in DNN training to find an appropriate physical image size (refers to pixel size) and technique with minimum computational costs. Next, deep Taylor decomposition was conducted to visualise the DNN decision and extract the characteristic features to reveal the spatial correlation of LC^3 and OPC. Then, the two-point correlation function and QNM were applied to quantify LC^3's microstructural refinement on both pores and solid phases, respectively. Finally, the pore morphological analysis was performed to represent pore deformation and hydration rate changes.

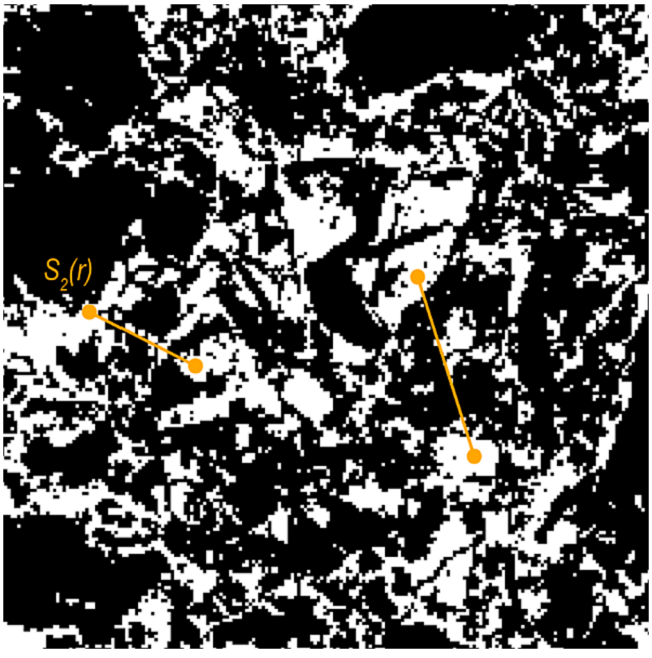

Fig. 2. Schematic of the two-point correlation function for a binary microstructure.

3.1. Microstructure virtualisation

BSE and micro-CT imaging techniques were applied to demonstrate the statistical pore size distribution of LC^3 and OPC. First of all, the 2D microstructural analysis of the OPC and LC^3 paste samples was conducted using high-resolution BSE images to understand the nano-/micro-scale microstructural modification effects of LC^3 with a pixel size of ≈0.07 μm. The original BSE images of LC^3 and OPC were binarised into solid and porous phases, shown in Fig. 3 (a), (b), (d) and (e). In order to visualise the microstructure of LC^3 and OPC, a pore diameter descriptor, d_p, was used to demonstrate equivalent pore diameters due to the irregular pore shapes observed in the cement microstructure, as indicated in equation (5):

$$d_p = 2 \times \sqrt{\frac{area}{\pi}} \quad (5)$$

The significant reduction in large pores in LC^3 compared with OPC can be seen in the equivalent pore diameter-based colour map illustrated in Fig. 3 (c) and (f). The largest equivalent pore diameter of LC^3 had ≈30% reduction compared with OPC, ≈25 μm and ≈35 μm, respectively. Furthermore, the equivalent pore diameters of LC^3 were mainly concentrated around < 5 μm. In contrast, many pores with equivalent pore diameters between 20 and 30 μm were observed in OPC, showing the denser microstructure of LC^3. The reduction in both the largest and the average equivalent pore diameters suggested a refining of the LC^3 microstructure.

The micro-CT images obtained from LC^3 and OPC were converted into virtual cement microstructure templates in order to assess the reliability of our work, as shown in Fig. 4 (a) and (b), respectively. Due to the limited resolution of the micro-CT, the finest pore diameter that can be captured was ≈0.7 μm. The micro-CT pore size distribution results showed a similar trend to the 2D BSE image analysis, indicating that the total pore volume of LC^3 was lower than that of OPC at 28 days of hydration, as shown in Fig. 4 (c). Compared with OPC, a significant reduction in large pores (equivalent pore diameter > 100 μm) can be observed in 28-day LC^3. Furthermore, the largest pore diameter of LC^3 was approximately 92% compared with that of OPC, being 234 μm and 253 μm, respectively, illustrating the denser microstructure of LC^3. This result demonstrated a similar trend obtained from the 2D image analysis, indicating the pore modifications of LC^3, especially the reduction in larger pores.

3.2. Deep learning-based microstructural characterisation

3.2.1. Influence of image size and resolution on DNN classification accuracy

The DNN-based characterisation was used to analyse the microstructure of the cement samples with different sized physical images and resolutions from BSE and micro-CT image datasets. As shown in Fig. 5 (a), classification accuracy grew with an increased physical size of the BSE and micro-CT images because more microstructural details were contained in each image, reflecting the microstructural differences between LC^3 and OPC. The classification accuracy stabilised after 81.12 × 81.12 μm with an accuracy of approximately 74% and 96% for the micro-CT and BSE images, respectively. Thus, for both BSE and micro-CT, images with an area of 81.12 × 81.12 μm contained nearly the same effective properties as the entire sample at this size.

Furthermore, 22% of the lower accuracy on micro-CT images could be mainly attributed to the limitation of resolution leading to a lack of

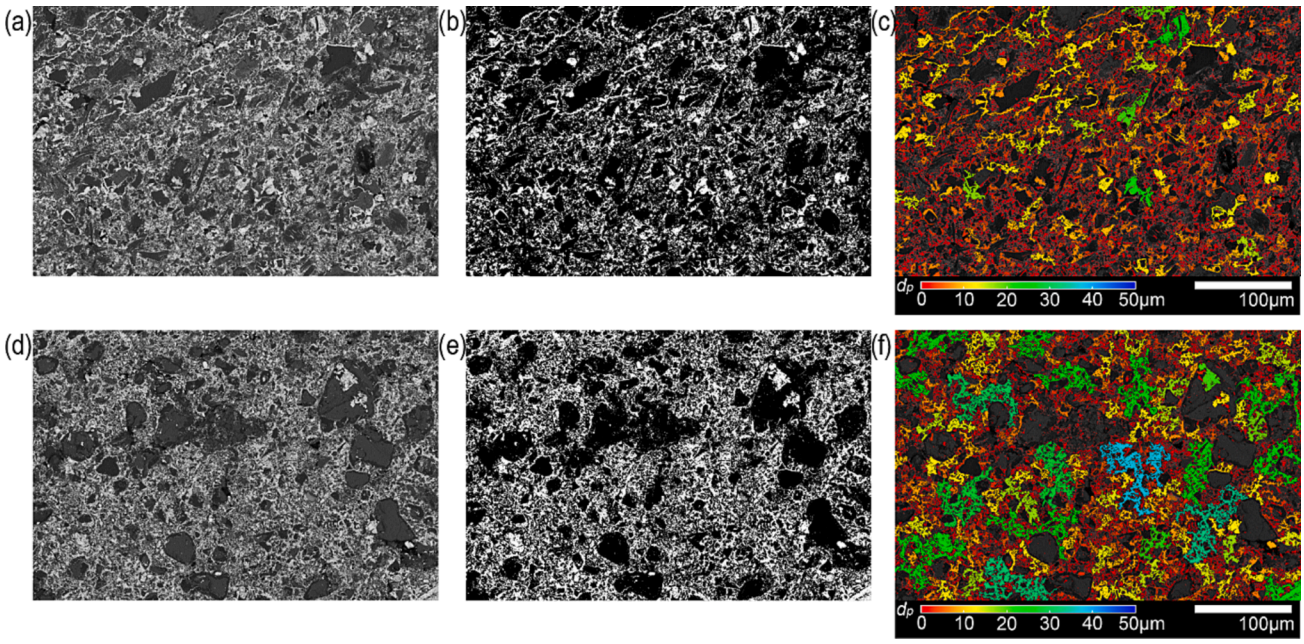

Fig. 3. Visualisation of BSE images. (a) Typical 28-day BSE image of LC^3. (b) Binarised BSE image of (a). (c) Equivalent pore diameter-based colour map of metal-intruded LC^3 based on (b). (d) Typical BSE image of 28-day OPC. (e) Binarised BSE-image of (d). (f) Equivalent pore diameter-based colour map of metal-intruded OPC based on (e).

detailed microstructural information at the nanoscale (from ~ 70 nm to ~ 700 nm in this case) compared with BSE images shown in Fig. 5 (b) and (c). This is because cementitious materials are known to have a scale-dependent fractal property [53]. The representative volume element (RVE), a critical parameter in building a sensible processing–structure–property connection to obtain insight underlying a material's behaviour, is the smallest volume representing the characteristics with nearly the same effective properties of the entire sample [15]. The representative features include not only solid phases and pores but also the statistical distribution and spatial positioning, leading to an RVE size multiple times larger than the largest particle size of the composite [19,54]. The BSE images with 81.12 × 81.12 μm can be considered as the RVE of 28-day LC^3 and OPC in this study. Therefore, only the categories of BSE image with a size of 81.12 × 81.12 μm were used in deep Tylor decomposition to represent the entire sample with the lowest costs for microstructural characterisation.

3.2.2. *Visualisation of the DNN via deep Taylor decomposition*

Deep Taylor decomposition, one of the most commonly used algorithms to visualise and demonstrate the decisions of a DNN, was conducted to assist in understanding the DNN decisions and explaining the microstructural refinement effects of LC^3. It is helpful to extract and visualise the decision of the DNN model because DNN prediction is like a 'black box' and hard to understand. Fig. 6 presented the process of the deep Tylor decomposition of DNN results using 81.12 × 81.12 μm categories. Relevance maps were generated to illustrate the relevance of each pixel in the images to visualise the DNN classification decisions, as shown in Fig. 6 (b). Features shown in the relevance map were recognised as the characteristic patterns of the binarised BSE image categories. The relevance map exhibits the characteristic features of characteristic patterns assisting in differentiating the LC^3 and OPC samples of the DNN. Considering the relative large-scale homogeneity of cement [55], characteristic patterns were consistently observed in the middle areas of the binarised BSE images.

As shown in Fig. 6 (b), the relevance maps are separated by red (relevant low-density regions or pores) and blue (relevant high-density regions or solid phases). It is worth noting that the central area of the images has a greater probability of featuring complete pore/pore clusters or solid phase structures. This particular attribute significantly aids the identification process of the DNN since the central regions frequently exhibit discernible and distinct characteristic patterns that can be effectively learned by the network. It can be seen that LC^3 had more relevant regions in high-density regions, whereas the most relevant areas of OPC were related to low-density regions. The pore clusters more likely appeared in low-density regions resulting in a relatively high porosity region [43,56]. In comparison with low-density regions, the high-density regions consisted of unhydrated cement and hydration products in both LC^3 and OPC, as well as fillers in LC^3 (i.e., LS) and the low reactivity materials in CC (i.e., muscovite and quartz). The pore clusters and solid phases are related to cement hydration because hydration products gradually grow on the surface of the solid phases and fill the pores during cement hydration [14]. Fig. 6 (c) represented the 70% most relevant area from Fig. 6 (b). These regions were then used to extract the characteristic features at corresponding regions from the original BSE images to form Fig. 6 (d). In Fig. 6 (d), the extracted features of LC^3 are mostly related to the solid phase, indicating that the solid phases of LC^3 have typical characteristics that distinguish them from OPC. In contrast, the extracted features of OPC are mostly pores, which is attributed to its higher porosity and different pore shapes. Specifically, OPC has more volume of pores with reduced solidity compared with LC^3, as described in Section 3.1.

Based on the 2000 extracted characteristic features of each cement type given in Fig. 6 (d), the hidden effects of spatial heterogeneity in the long-range correlation were demonstrated by extracting high-dimensional characteristic patterns, as shown in Fig. 7. The characterisation indicating the probability of navigating the shared pores at various locations in OPC and LC^3 is illustrated in Fig. 7 (a) and (b), respectively. Three typical heatmaps are given for each type of cement to signify the general changes in characteristic patterns. The differences in the general trend of the characteristic patterns between LC^3 and OPC revealed a deviation between strength and porosity based on the point-set topological theory [57]. The high-intensity regions in the heatmaps demonstrated increased topological parameters, such as pore compactness and connectedness [58], and consistency of the distribution of the pores at the nanoscale. These parameters could influence stiffness and strength performance [59]. It can be seen that all heatmaps of LC^3 show

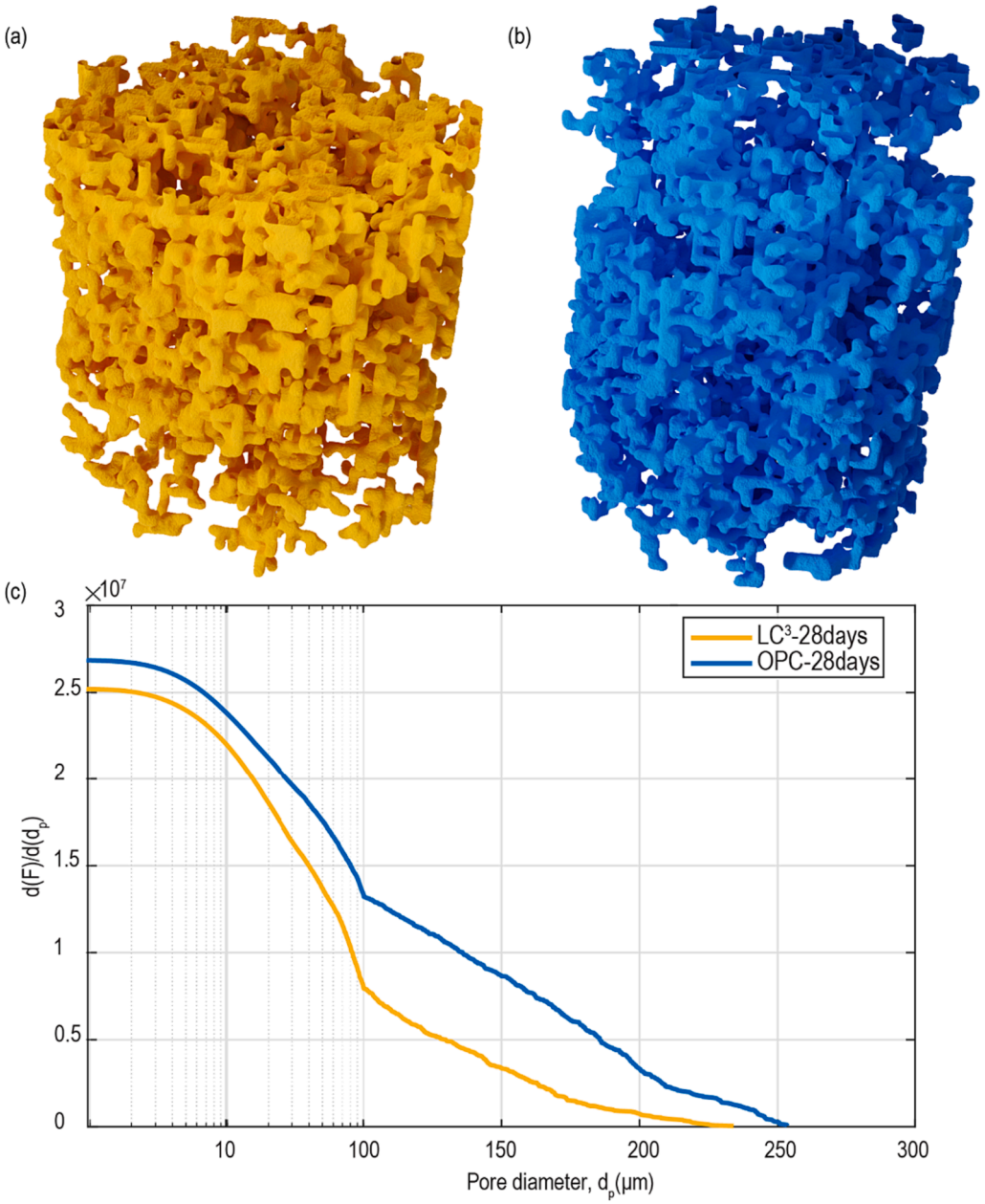

Fig. 4. Virtualisation of reconstructed microstructure from the original micro-CT images of (a) LC^3 and (b) OPC. (c) Pore size distribution of LC^3 and OPC at 7 and 28 days from analysis based on micro-CT images.

a lower probability of the occurrence of continuous pores and less connectivity with pores compared with OPC. The reduced pore connectivity and pore occurrence possibility resulted in a more refined microstructure with a higher apparent matrix densification of LC^3, and thus provided better mechanical and durability-related performance [60]. In contrast, the high probability of occurrence of OPC's solid phases (black regions in the heatmap) was most likely finer than 2.5 μm, as illustrated in Fig. 7 (a). However, LC^3 had more connected larger solid areas in the heatmap, which implies minimizing stress concentrations to form a high-connectivity force-chain network [61] and finally contributed to superior mechanical properties and durability-related performance. In addition, the lower average solid particle size in LC^3 resulted in a higher surface area that could also contribute to a higher hydration rate compared with OPC. This is consistent with the hydration and mechanical performance improvements mentioned in the literature [11–13].

3.3. Spatial distribution characterisation

The two-point correlation indicates the probability of spatial distribution between two random pixels from pore clusters. Ideally, the two-point correlation result should equal the porosity when correlation distance $r = 0$. With increased distance between two random pixels, the two-point correlation result will decrease and finally vibrate around the square of the porosity [62]. In Fig. 8 (a) and (b), the porosities calculated by the two-point correlation function of the LC^3 and OPC images were ≈0.30 and 0.34, respectively. These values were consistent with those revealed in the image-based pore size distribution results, which also proved the reliability of the two-point correlation function used in this study. Furthermore, the maximum correlation distance is independent of total porosity [63,64]. In this study, the distances at which the two-point correlation function maintained stable for LC^3 and OPC were calculated at ≈20 μm and 30 μm, respectively. The 33% lower maximum correlation distance stabilising the two-point correlations in 28-day LC^3

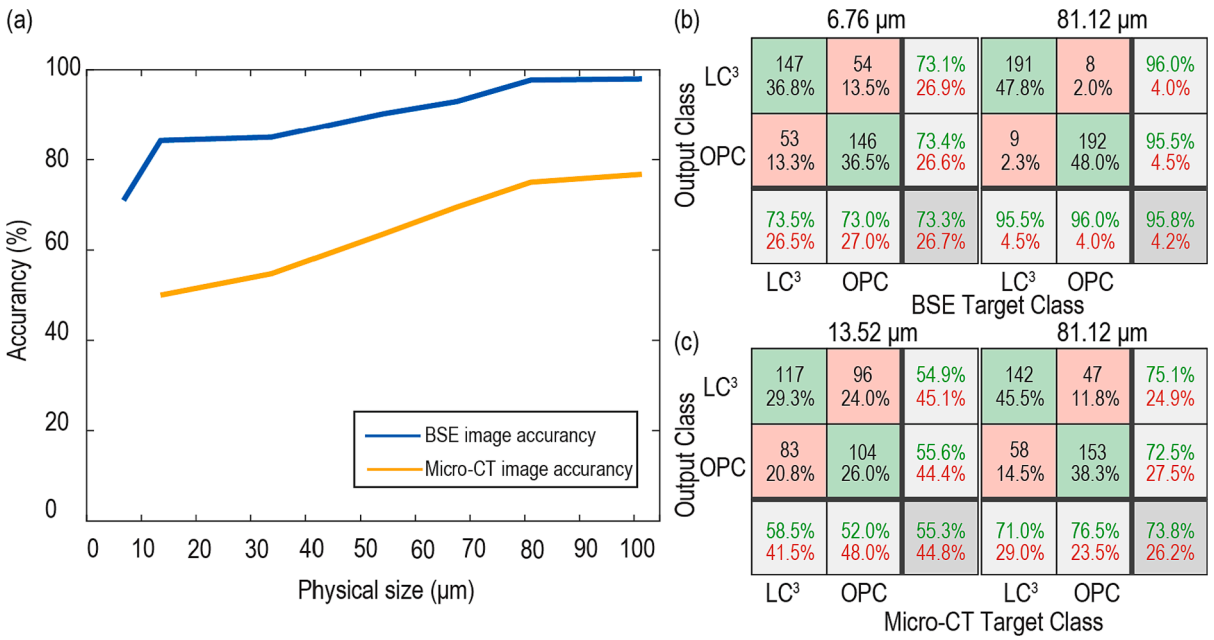

Fig. 5. (a) Classification accuracy of the test datasets on BSE and micro-CT images with various physical sizes using the same DNN. (b) Examples of DNN classification confusion matrix of BSE binary images. (c) Examples of DNN classification confusion matrix of micro-CT binary images. In (b) and (c), the green background and number represented the images accurately identified and classification accuracy, respectively, whereas the red background and numbers represented the images that failed to be classified and inaccuracy. (For interpretation of the references to colour in this figure legend, the reader is referred to the web version of this article.)

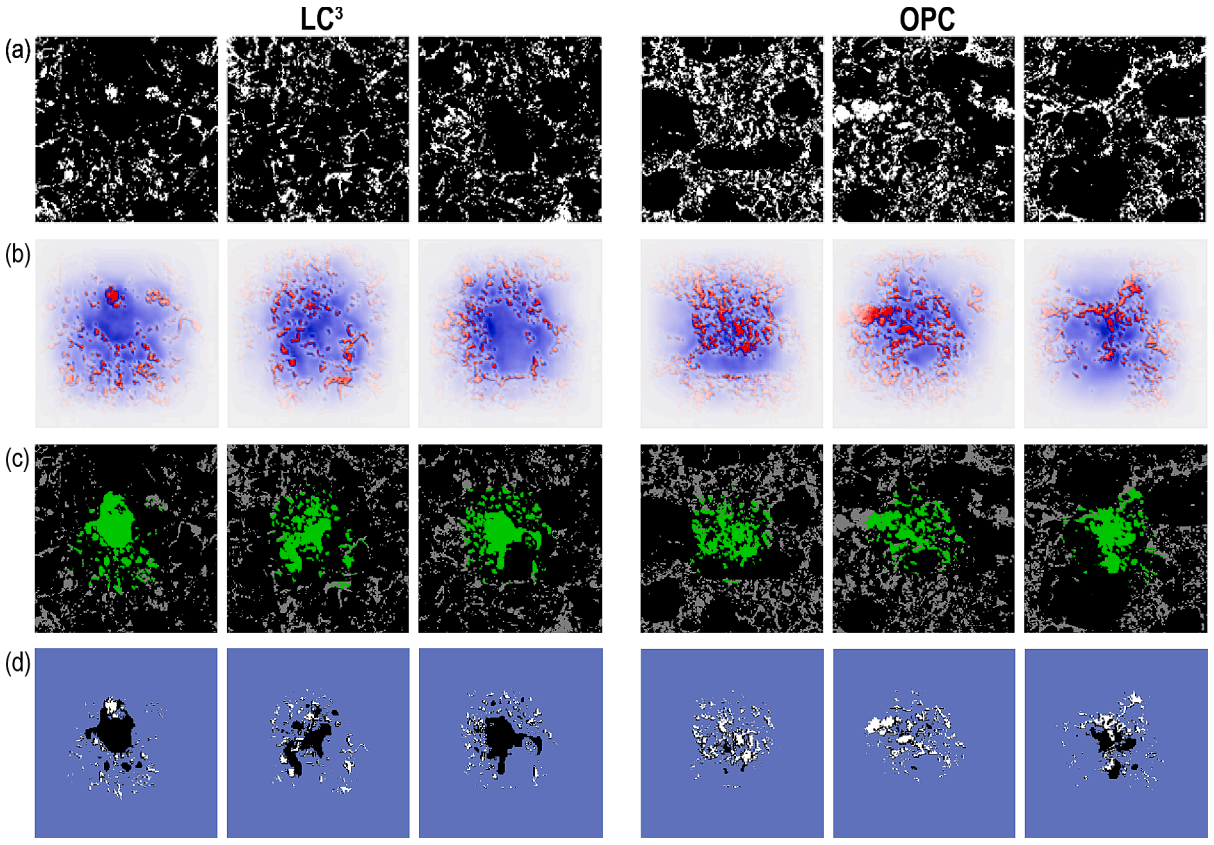

Fig. 6. Visualisation and characterisation feature extraction via deep Taylor decomposition. (a) Typical BSE cross-section images of LC^3 and OPC with a physical size of 81.12 × 81.12 μm. (b) Locations of characteristic features relevant to DNN decision where red represents low-density areas or pores, and blue represents high-density areas or solid phases. (c) Locations of the characteristic regions with 70% of the total relevance in characteristic features. (d) Extracted characteristic features at the corresponding areas of (a). (For interpretation of the references to colour in this figure legend, the reader is referred to the web version of this article.)

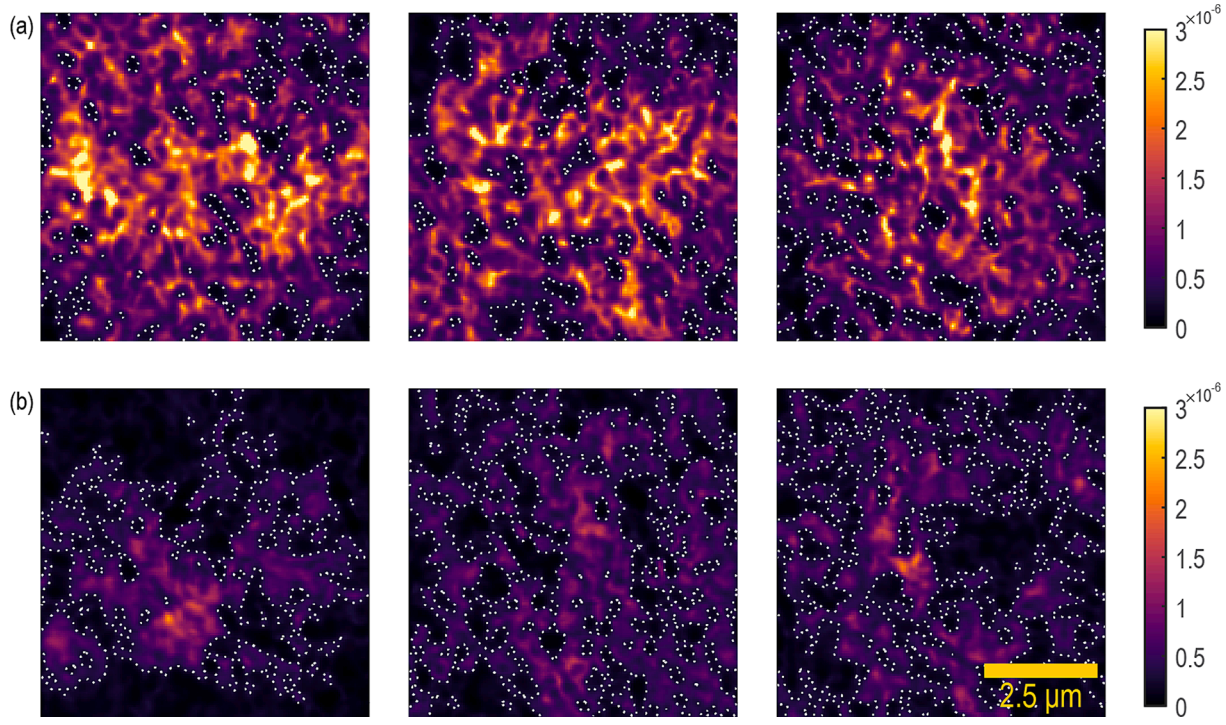

Fig. 7. Typical heatmaps of the shared characteristic pattern changes of (a) OPC and (b) LC^3. The heatmap was achieved by iterating over the most similar shared characteristics patterns by deep Taylor decomposition.

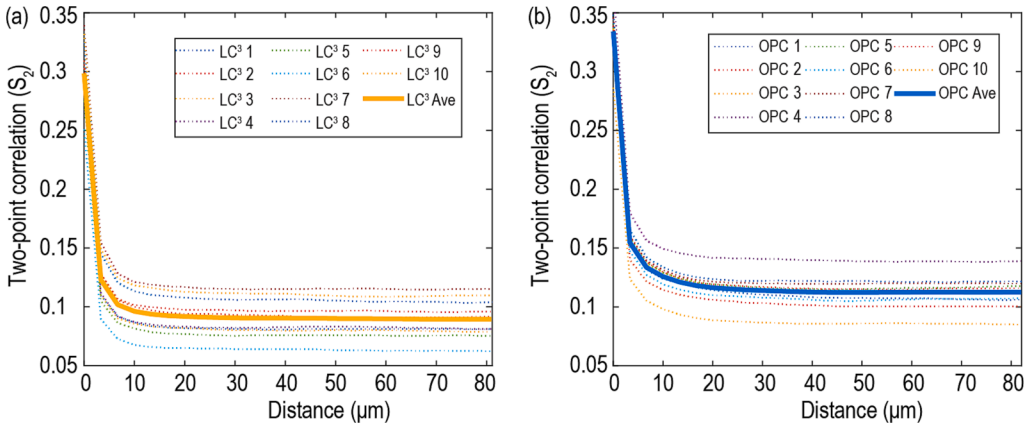

Fig. 8. Two-point correlation functions of the microstructure for cement samples with different physical distances in (a) 28-day LC^3 and (b) 28-day OPC images.

can infer that LC^3 has a smaller RVE size. The results are possibly due to an increasing packing density in the microstructure of LC^3, where the small particle size of CC and LS filled the pores and voids in the cement without loosening the packing of cement [65]. The reduced distance stabilising the two-point correlations is also likely related to the pozzolanic reaction and the synergetic reaction between CC and LS, contributing to more hydration products and thus a denser and more uniform microstructure than OPC.

To further understand the spatial correlation between the solid phases of LC^3 and OPC pastes, PeakForce QNM was used to evaluate the nanomechanical properties. Knowing the microstructural densification and uniformity are also influenced by the type and volume of the hydration products and unhydrated solid phases. Fig. 9 presents the nanomechanical properties (E) of 28-day LC^3 and OPC pastes with a scanning area of 20 × 20 μm by PeakForce QNM. The contour maps of E of LC^3 and OPC are illustrated in Fig. 9 (a) and (b). The main phases in both cement pastes included defects and pores (DP), low-density hydration products (LD), high-density hydration products (HD), and unhydrated grains (UG). The unhydrated metakaolin (MK) only present in LC^3 had a slightly lower E than LD [66]. Due to the high demand for surface flatness, the defects and pores were filled with epoxy with the impregnation process to maintain the flatness of the sample surface. DP was still accurately identified from the solid phases with limited influence on the accuracy of QNM because epoxy has a much lower E than other solid phases [25].

The statistic probability distribution of E in the solid phases was fitted via multimodal Gaussian distribution with $R^2 > 0.995$ to identify the fractions of different solid phases, as indicated in Fig. 9 (c) and (d). In Fig. 9 (e), it can be seen from the characteristic E ranges that LC^3 had a>2-fold low-density volume than OPC, which could be attributed to the unhydrated MK in CC. According to the existing literature, the hydration rate of 15% MK is ≈33% [67]. Therefore, ≈10% unhydrated MK combined with low-density hydrates in LC^3, where E ranged from 15 to 20 GPa. The presence of CC and LS promoted hydration because of the

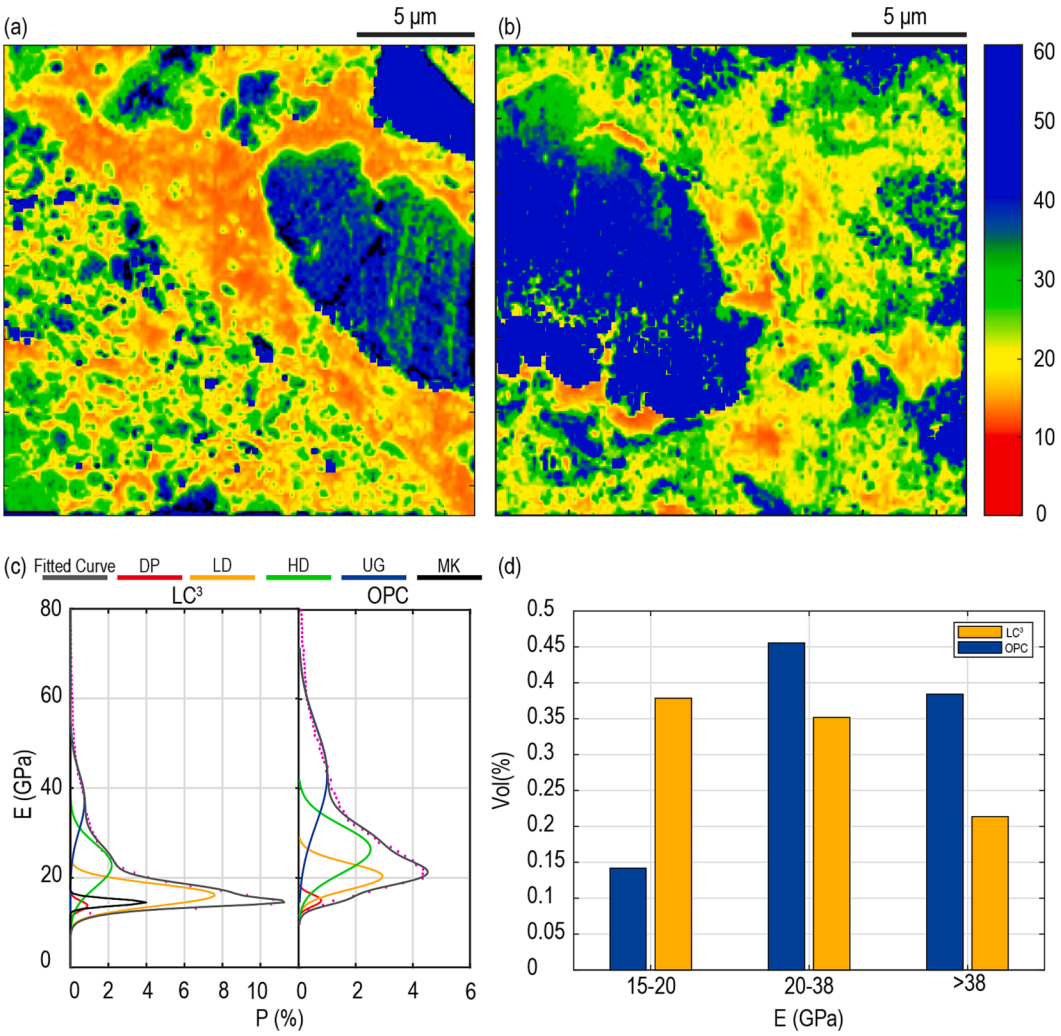

Fig. 9. PeakForce QNM contour maps of Young's modulus (E) of (a) LC^3 and (b) OPC. Statistical probability distribution of E of (c) LC^3 and OPC. (d) Three characteristic E ranges of tested samples.

nucleation effect, whereby MK provides various nucleation sites on its surface, forming carboaluminates [12]. Due to the layered structure of MK, these carboaluminates are deposited in the pore space with a similar deposition mechanism to LD [68]. Furthermore, due to the high clinker substitution ratio, the proportion of UG decreased accordingly in LC^3, leading to only 60% of the volume of UG compared with OPC. More areas were found in LC^3 to have an E between 15 and 38 GPa, indicating a minor variation of E and thus a more uniform cement microstructure. A more uniform microstructure could increase mechanical strength while decreasing the stress concentration in the LC^3 paste [25], which is also consistent with the DNN results, indicating that LC^3 has a higher hydration rate than OPC. The results have significant implications for the design of LC^3 concrete, as they provide valuable insights for optimising its mechanical properties and improving durability performance. Furthermore, it is worth mentioning that in cases where the mean strength surpasses the threshold required to counteract the localisation effect, a multi-scale analysis can be pursued to delve deeper into the subject. This analysis could involve examining the comparison between the micro-scale and *meso*-scale properties [38,69,70], providing valuable insights into the material behaviour at different scales.

3.4. Pore morphological characterisation

In order to evaluate the localised pore structure differences between LC^3 and OPC, the pore morphology descriptor, solidity, was used to represent pore deformation and hydration rate changes from original BSE images. Solidity is influenced by the growth of hydration products [26]. Fig. 10 (a) and (b) are a scatter diagram and the average statistical distribution against the equivalent pore diameter of solidity in LC^3 and OPC, respectively. The x-axis of OPC was shifted to the right to observe Fig. 10 (b) clearly. The average solidity was similar and indicated a downward trend for both OPC and LC^3 due to hydration and packing. Noting that the average solidity of LC^3 was slightly lower than that of OPC. This is mainly attributed to the combination of the pozzolanic reaction of MK in the CC and the synergetic reaction between LS and CC, providing nucleation sites to form carboaluminates and external C-(A)-S-H formation [29,68]. A greater variety and quantity of hydration products and a higher hydration rate could lead to slight changes in the cement microstructure, resulting in higher pore surface areas of LC^3. These extra hydration products are deposited on the surface of the solid phases and segment larger pores into finer pores, resulting in pore modifications in LC^3, consistent with the pore size distribution results shown in Figs. 3 and 4. It can be seen, however, that LC^3 has a slightly higher solidity after 6 μm compared with OPC, which can be attributed to unhydrated LS and low-reactivity solid phases in CC, such as muscovite and quartz. These low-reactivity solid phases mainly act as fillers and undergo little or no hydration reactions [71]. According to the pore size distribution results, LC^3 has less volume of larger pores, inferring the slightly higher solidity of larger pores had less influence on the overall microstructural refinement. The pore morphological analysis

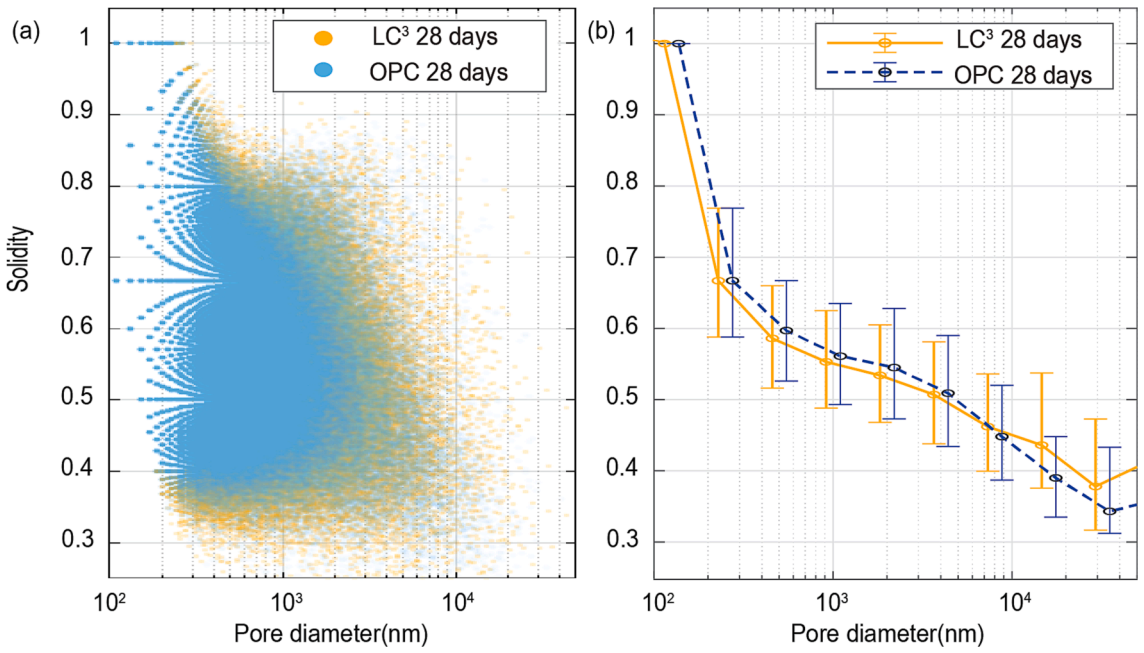

Fig. 10. Shape descriptor, solidity, of LC^3 and OPC. (a) Scatter diagram of 28-day LC^3 and OPC and (b) statistic curve of the average solidity distribution.

also suggested that the cylindrical pore assumption in Washburn's equation [45] of mercury intrusion porosimetry analysis could potentially complement the shape descriptor to improve the accuracy of future microstructural characterisation of cementitious materials in further research.

4. Conclusions

Based on the results presented here, we have described microstructural refinement mechanisms on pore size, the spatial correlation of pores and cement composites, and the solidity of 28-day LC^3 through a deep learning approach combined with image-based microstructure characterisation. The salient findings are shown below.

- The BSE images were adopted in deep learning characterisation, which increased ≈20% accuracy by capturing the nano-features compared to micro-CT at corresponding physical image size. A physical image size of 81.12 × 81.12 μm was used in DNN training with the optimised efficiency for localised microstructural characterisation.
- Based on the decomposition of DNN, LC^3 had a lower probability of occurring connected pores and pore clusters than OPC. On the other hand, LC^3 had a higher likelihood of forming connected larger solid areas than OPC, which minimised stress concentrations and led to a higher apparent matrix densification. Both of these contributed to improved mechanical properties and superior durability-related performance.
- From the two-point correlation analysis, LC^3 had a 33% lower maximum correlation distance than OPC, demonstrating that LC^3 possessed a smaller RVE size and increased packing density in its microstructure. Based on nanomechanical property mapping, LC^3 had a more uniform microstructure with 40% fewer unhydrated grains compared to OPC, which increases the mechanical strength while decreasing the stress concentration in LC^3 paste.
- LC^3 had lower average solidity than OPC, with an equivalent pore diameter < 6 μm, illustrating greater pore deformation and hydration rate, which can be attributed to the formation of carboaluminates and external C-(A)-S-H from the pozzolanic reaction and synergetic reactions between CC and LS. The slightly higher solidity after 6 μm may be attributed to unhydrated LS and low-reactivity phases in CC.

In summary, we reveal the microstructural refinement mechanisms of 28-day LC^3 and lay the basis for localised microstructural characterisation of cementitious materials. By understanding the microstructural refinement mechanisms of LC^3, such as microstructure uniformity leading to decreased stress concentration, practitioners can make informed decisions in the design and future developments of LC^3-based concrete. Additionally, these findings contribute to establishing the structure–property relationship in LC^3, thereby complementing traditional microstructural analyses of cementitious materials.

Declaration of Competing Interest

The authors declare that they have no known competing financial interests or personal relationships that could have appeared to influence the work reported in this paper.

Data availability

Data will be made available on request.

Acknowledgements

The authors are grateful for the financial support of the Australian Research Council (IH150100006) in conducting this study. The authors appreciate the kind support in providing calcined clay from Sinoma International Engineering Co., Ltd. through the National Key R&D Program of China (2016YFE0206100 and 2017YFB0310905). The authors acknowledge Dr Kwesi Sagoe-Crentsil and Yanming Liu from Monash University and the use of facilities within the Monash Centre for Electron Microscopy (MCEM) and Melbourne Centre for Nanofabrication (MCN).

References

[1] S. Antiohos, K. Maganari, S. Tsimas, Evaluation of blends of high and low calcium fly ashes for use as supplementary cementing materials, Cem. Concr. Compos. 27 (3) (2005) 349–356.

[2] International Energy Agency and The Cement Sustainability Initiative, *Technology Roadmap: Low-Carbon Transition in the Cement Industry*. 2018, Paris.
[3] M. Guo, et al., Performance evaluation of recycled aggregate concrete incorporating limestone calcined clay cement (LC3), J. Clean. Prod. 366 (2022), 132820.
[4] Z. Liang, et al., Improving recycled aggregate concrete by compression casting and nano-silica, Nanotechnol. Rev. 11 (1) (2022) 1273–1290.
[5] Sui, H., et al., *The investigation of limestone calcined clay cement: A review*, in *In: WEC2019: World Engineers Convention 2019. Melbourne: Engineers Australia, 2019: 750-763.* 2019, Engineers Australia.
[6] S. Sánchez Berriel, A. Favier, E. Rosa Domínguez, I.R. Sánchez Machado, U. Heierli, K. Scrivener, F. Martirena Hernández, G. Habert, Assessing the environmental and economic potential of Limestone Calcined Clay Cement in Cuba, J. Clean. Prod. 124 (2016) 361–369.
[7] R. Fernandez, F. Martirena, K.L. Scrivener, The origin of the pozzolanic activity of calcined clay minerals: A comparison between kaolinite, illite and montmorillonite, Cem. Concr. Res. 41 (1) (2011) 113–122.
[8] H. Wang, et al., Synergistic effects of supplementary cementitious materials in limestone and calcined clay-replaced slag cement, Constr. Build. Mater. 282 (2021), 122648.
[9] C. Lian, Y. Zhuge, S. Beecham, The relationship between porosity and strength for porous concrete, Constr. Build. Mater. 25 (11) (2011) 4294–4298.
[10] H. Du, S. Dai Pang, High-performance concrete incorporating calcined kaolin clay and limestone as cement substitute, Constr. Build. Mater. 264 (2020), 120152.
[11] K. Scrivener, F. Martirena, S. Bishnoi, S. Maity, Calcined clay limestone cements (LC3), Cem. Concr. Res. 114 (2018) 49–56.
[12] H. Sui, P. Hou, Y. Liu, K. Sagoe-Crentsil, F. Basquiroto de Souza, W. Duan, Limestone calcined clay cement: mechanical properties, crystallography, and microstructure development, J. Sustainable Cement-Based Mater. 12 (4) (2023) 427–440.
[13] F. Zunino, K. Scrivener, Microstructural developments of limestone calcined clay cement (LC3) pastes after long-term (3 years) hydration, Cem. Concr. Res. 153 (2022), 106693.
[14] H.F. Taylor, Cement chemistry, Vol. 2, Thomas Telford London, 1997.
[15] R. Bostanabad, Y. Zhang, X. Li, T. Kearney, L.C. Brinson, D.W. Apley, W.K. Liu, W. Chen, Computational microstructure characterization and reconstruction: Review of the state-of-the-art techniques, Prog. Mater Sci. 95 (2018) 1–41.
[16] S. Torquato, H. Haslach Jr, Random heterogeneous materials: microstructure and macroscopic properties, Appl. Mech. Rev. 55 (4) (2002) B62–B63.
[17] J. Miao, L. Lu, J. Jiang, Reinforcement of ultra-low dosage of polycarboxylate ether (PCE) grafted nano-silica sol to the mechanical and durable properties of cement mortar, J. Mater. Res. Technol. 19 (2022) 3646–3657.
[18] A. Jenni, L. Holzer, R. Zurbriggen, M. Herwegh, Influence of polymers on microstructure and adhesive strength of cementitious tile adhesive mortars, Cem. Concr. Res. 35 (1) (2005) 35–50.
[19] J. Lin, et al., Microstructure of graphene oxide–silica-reinforced OPC composites: Image-based characterization and nano-identification through deep learning, Cem. Concr. Res. 154 (2022), 106737.
[20] A. Gokhale, A. Tewari, H. Garmestani, Constraints on microstructural two-point correlation functions, Scr. Mater. 53 (8) (2005) 989–993.
[21] D.A. Lange, H.M. Jennings, S.P. Shah, Image analysis techniques for characterization of pore structure of cement-based materials, Cem. Concr. Res. 24 (5) (1994) 841–853.
[22] Y. Liu, et al., Digital concrete modelling: an alternative approach to microstructural pore analysis of cement hydrates, Constr. Build. Mater. 303 (2021), 124558.
[23] P.B. Corson, Correlation functions for predicting properties of heterogeneous materials. I. Experimental measurement of spatial correlation functions in multiphase solids, J. Appl. Phys. 45 (7) (1974) 3159–3164.
[24] P.B. Corson, Correlation functions for predicting properties of heterogeneous materials. II. Empirical construction of spatial correlation functions for two-phase solids, J. Appl. Phys. 45 (7) (1974) 3165–3170.
[25] W. Wang, et al., Graphene oxide-reinforced thin shells for high-performance, lightweight cement composites, Compos. B Eng. 235 (2022), 109796.
[26] S.J. Chen, W.G. Li, C.K. Ruan, K. Sagoe-Crentsil, W.H. Duan, Pore shape analysis using centrifuge driven metal intrusion: Indication on porosimetry equations, hydration and packing, Constr. Build. Mater. 154 (2017) 95–104.
[27] Y. Liu, et al., Evolution of tricalcium silicate (C3S) hydration based on image analysis of microstructural observations obtained via Field's metal intrusion, Mater Charact 181 (2021), 111457.
[28] S.R. Niezgoda, Y.C. Yabansu, S.R. Kalidindi, Understanding and visualizing microstructure and microstructure variance as a stochastic process, Acta Mater. 59 (16) (2011) 6387–6400.
[29] F. Avet, E. Boehm-Courjault, K. Scrivener, Investigation of CASH composition, morphology and density in Limestone Calcined Clay Cement (LC3), Cem. Concr. Res. 115 (2019) 70–79.
[30] M. Sharma, et al., Limestone calcined clay cement and concrete: A state-of-the-art review, Cem. Concr. Res. 149 (2021), 106564.
[31] I.M. Bernal, et al., Phase and microstructure evolutions in LC3 binders by multi-technique approach including synchrotron microtomography, Constr. Build. Mater. 300 (2021), 124054.
[32] Avet, F.H., Investigation of the grade of calcined clays used as clinker substitute in Limestone Calcined Clay Cement (LC3). 2017, EPFL.
[33] H. Lee, et al., Unsupervised feature learning for audio classification using convolutional deep belief networks. Advances in Neural Information Processing Systems, 2009.
[34] G.E. Hinton, R.R. Salakhutdinov, Reducing the dimensionality of data with neural networks, Science 313 (5786) (2006) 504–507.
[35] Y. LeCun, Y. Bengio, G. Hinton, Deep learning, Nature 521 (7553) (2015) 436–444.
[36] J. Guo, et al., Estimating cement compressive strength using three-dimensional microstructure images and deep belief network, Eng. Appl. Artif. Intel. 88 (2020), 103378.
[37] X. Li, Z. Liu, S. Cui, C. Luo, C. Li, Z. Zhuang, Predicting the effective mechanical property of heterogeneous materials by image based modeling and deep learning, Comput. Methods Appl. Mech. Eng. 347 (2019) 735–753.
[38] R. Lorenzoni, et al., Semantic segmentation of the micro-structure of strain-hardening cement-based composites (SHCC) by applying deep learning on micro-computed tomography scans, Cem. Concr. Compos. 108 (2020), 103551.
[39] I. Goodfellow, Y. Bengio, A. Courville, Deep Learning, MIT Press, 2016.
[40] W. Aleadelat, K. Aledealat, K. Ksaibati, Estimating pavement roughness using a low-cost depth camera, Int. J. Pavement Eng. 23 (14) (2022) 4923–4930.
[41] G. Montavon, S. Lapuschkin, A. Binder, W. Samek, K.-R. Müller, Explaining nonlinear classification decisions with deep taylor decomposition, Pattern Recogn. 65 (2017) 211–222.
[42] G. Montavon, W. Samek, K.-R. Müller, Methods for interpreting and understanding deep neural networks, Digital Signal Process. 73 (2018) 1–15.
[43] W. Wang, S.J. Chen, W. Duan, K. Sagoe-Crentsil, C.S.N. Pathirage, L. Li, J. Lin, Revealing microstructural modifications of graphene oxide-modified cement via deep learning and nanoporosity mapping: implications for structural materials' performance, ACS Applied Nano Materials 5 (5) (2022) 7092–7102.
[44] S. Australia, As 3972 general purpose and blended cements, Standards Australia, Sydney, Australia, 2010.
[45] E.W. Washburn, Note on a Method of Determining the Distribution of Pore Sizes in a Porous Material, Proc. Natl. Acad. Sci. U.S.A. 7 (4) (1921) 115–116.
[46] Ferreira, T. and W. Rasband, *ImageJ user guide*. ImageJ/Fiji, 2012. **1**: p. 155-161.
[47] U. Gonzales-Barron, F. Butler, A comparison of seven thresholding techniques with the k-means clustering algorithm for measurement of bread-crumb features by digital image analysis, J. Food Eng. 74 (2) (2006) 268–278.
[48] P. Panwar, G. Gopal, R. Kumar, Image segmentation using K-means clustering and thresholding, Image 3 (05) (2016) 1787–1793.
[49] X. Zheng, Q. Lei, R. Yao, Y. Gong, Q. Yin, Image segmentation based on adaptive K-means algorithm, EURASIP J. Image Video Process. 2018 (1) (2018).
[50] S.J. Chen, Y. Tian, C.Y. Li, W.H. Duan, A new scheme for analysis of pore characteristics using centrifuge driven non-toxic metal intrusion, Geomech. Geophys. Geo-Energy Geo-Resour. 2 (3) (2016) 173–182.
[51] Y. Hu, Y.A. Li, C.K. Ruan, J.L. Lin, S.J. Chen, H.M. Tang, W.H. Duan, Transformation of pore structure in consolidated silty clay: New insights from quantitative pore profile analysis, Constr. Build. Mater. 186 (2018) 615–625.
[52] F.R. Velasco, Thresholding Using the ISODATA Clustering Algorithm, Maryland Univ College Park Computer Science Center, 1979.
[53] Q. Zeng, K. Li, T. Fen-Chong, P. Dangla, Surface fractal analysis of pore structure of high-volume fly-ash cement pastes, Appl. Surf. Sci. 257 (3) (2010) 762–768.
[54] Q. Wu, T. Rougelot, N. Burlion, X. Bourbon, Representative volume element estimation for desorption isotherm of concrete with sliced samples, Cem. Concr. Res. 76 (2015) 1–9.
[55] A. Bouguerra, A. Ledhem, F. de Barquin, R.M. Dheilly, M. Quéneudec, Effect of microstructure on the mechanical and thermal properties of lightweight concrete prepared from clay, cement, and wood aggregates, Cem. Concr. Res. 28 (8) (1998) 1179–1190.
[56] P.D. Tennis, H.M. Jennings, A model for two types of calcium silicate hydrate in the microstructure of Portland cement pastes, Cem. Concr. Res. 30 (6) (2000) 855–863.
[57] Simmons, G.F., Introduction to topology and modern analysis. 1963: Tokyo.
[58] Wei, W., Development of high-performance cementitious composites: bioinspired design, digital fabrication, and ai-based characterization. 2019.
[59] J. Gao, Z. Luo, H. Li, L. Gao, Topology optimization for multiscale design of porous composites with multi-domain microstructures, Comput. Methods Appl. Mech. Eng. 344 (2019) 451–476.
[60] M. Antoni, J. Rossen, F. Martirena, K. Scrivener, Cement substitution by a combination of metakaolin and limestone, Cem. Concr. Res. 42 (12) (2012) 1579–1589.
[61] C. Giusti, L. Papadopoulos, E.T. Owens, K.E. Daniels, D.S. Bassett, Topological and geometric measurements of force-chain structure, Phys. Rev. E 94 (3) (2016), 032909.
[62] C.L.Y. Yeong, S. Torquato, Reconstructing random media, Phys. Rev. E 57 (1) (1998) 495–506.
[63] A.B. Harris, Effect of random defects on the critical behaviour of Ising models, J. Phys. C Solid State Phys. 7 (9) (1974) 1671–1692.
[64] A. Tewari, A.M. Gokhale, J.E. Spowart, D.B. Miracle, Quantitative characterization of spatial clustering in three-dimensional microstructures using two-point correlation functions, Acta Mater. 52 (2) (2004) 307–319.
[65] A. Kwan, J. Chen, Adding fly ash microsphere to improve packing density, flowability and strength of cement paste, Powder Technol. 234 (2013) 19–25.
[66] F. Pelisser, E.L. Guerrino, M. Menger, M.D. Michel, J.A. Labrincha, Micromechanical characterization of metakaolin-based geopolymers, Constr. Build. Mater. 49 (2013) 547–553.
[67] C.-S. Poon, L. Lam, S.C. Kou, Y.-L. Wong, R. Wong, Rate of pozzolanic reaction of metakaolin in high-performance cement pastes, Cem. Concr. Res. 31 (9) (2001) 1301–1306.
[68] T. Sato, F. Diallo, Seeding effect of nano-CaCO3 on the hydration of tricalcium silicate, Transp. Res. Rec. 2141 (1) (2010) 61–67.

[69] T.-S. Han, et al., Multi-scale analysis framework for predicting tensile strength of cement paste by combining experiments and simulations, Cem. Concr. Compos. 139 (2023), 105006.
[70] J. Li, et al., Micromechanics of engineered cementitious composites (ECC): A critical review and new insights, Constr. Build. Mater. 362 (2023), 129765.
[71] H. Moosberg-Bustnes, B. Lagerblad, E. Forssberg, The function of fillers in concrete, Mater. Struct. 37 (2) (2004) 74–81.